

Using the viscoelastic relaxation of large impact craters to study the thermal history of Mars



Saman Karimi^{a,*}, Andrew J. Dombard^a, Debra L. Buczkowski^b, Stuart J. Robbins^c,
Rebecca M. Williams^d

^aThe Department of Earth and Environmental Sciences, University of Illinois at Chicago, 845 W. Taylor St., SES (MC-186), Chicago, IL 60607, USA

^bPlanetary Exploration Group, Space Department, Johns Hopkins University Applied Physics Laboratory, MS 200-W230, 11100 Johns Hopkins Road, Laurel, MD 20723, USA

^cSouthwest Research Institute, 1050 Walnut St., Suite 300, Boulder, CO 80309, USA

^dPlanetary Science Institute, 1700 East Fort Lowell, Suite 106, Tucson, AZ 85719, USA

ARTICLE INFO

Article history:

Received 17 June 2015

Revised 15 February 2016

Accepted 23 February 2016

Available online 2 March 2016

Keywords:

Mars

Geophysics

Thermal histories

ABSTRACT

We simulate the long-term deformation of Martian craters and investigate the role of lower crustal flow in the evolution of surface and subsurface topography. Using the finite element method and a viscoelastic rheological model, we model the deformation of more than 30 large craters and Quasi-Circular Depressions (QCDs), in the diameter range of ~200–500 km, in both the Northern Lowlands and Southern Highlands. We determine the most appropriate background heat fluxes that produce the current topography beneath the impacts at the crust–mantle boundary (ranges from 40 to ~90 mW m⁻²). Our study shows that a higher background heat flux leads to more relaxation at the surface and subsurface. By applying various viscous creep parameters for hydrous and anhydrous rheologies, we demonstrate that Mars's interior is wet to a certain degree, which is consistent with other estimates. Since craters and QCDs are distributed fairly equally on the surface of the Red Planet, this study provides a less regionally biased picture of the thermal history of early Mars than in previous studies. Based on our results, the ancient average background heat flux in the Northern Lowlands was higher than that of the Southern Highlands, which could indicate that whatever process formed the crustal dichotomy had a thermal signature at least through the middle Noachian.

© 2016 Elsevier Inc. All rights reserved.

1. Introduction

Many previous studies of Mars have looked at the thermal history of the planet (e.g., Comer et al., 1985; Anderson and Grimm, 1998; McGovern et al., 2001, 2002, 2004; Montesi and Zuber, 2003; Watters and McGovern, 2006; Mohit and Phillips, 2006; Dombard and Phillips, 2010) because heat is the engine that drives a planet's geological evolution. There are, however, issues associated with these previous studies that may limit their applicability. These studies are limited to a few specific geographical locations because they required an identifiable load on the lithosphere (e.g., the Tharsis Montes, Vallis Marineris, etc.); therefore, there is limited information about any regional variations of the Martian heat flux. For instance, it is hard to determine systematic differences between various locations of Mars such as the Northern Lowlands, the Southern Highlands, under the polar caps, and Tharsis. Thus,

any conclusions of thermal history derived from these studies may be regionally biased and may not capture the background thermal state of the planet. Fig. 1 shows a compilation of the previous studies and displays model estimates of Martian heat flux versus time. There exists the potential that past geodynamically determined estimates of heat flux (boxes in the figure) might not be regionally representative, and these estimates (and their associated errors) cannot reliably distinguish between thermal models of Mars. There has never been an in situ measurement of Martian heat flux on its surface (though the InSight mission will change that for at least one place on Mars [Banerdt et al., 2012]); therefore, indirect measurement/modeling is key to revealing the thermal history of Mars. Here, we model the lithospheric deformation associated with large ancient Martian impact features, which thus may provide a geographically less biased tracer of the thermal history of Mars.

The work of Neumann et al. (2004) on Martian crustal thickness revealed that the mantle is uplifted beneath many large craters, likely as a result of the collapse of the transient crater immediately after the impact (e.g., Melosh, 1989; Wicczorek and Phillips, 1999). Sufficiently thick crust and high temperatures in the lower crust

* Corresponding author. Tel.: +1 312 9724010.
E-mail address: mkarim5@uic.edu (S. Karimi).

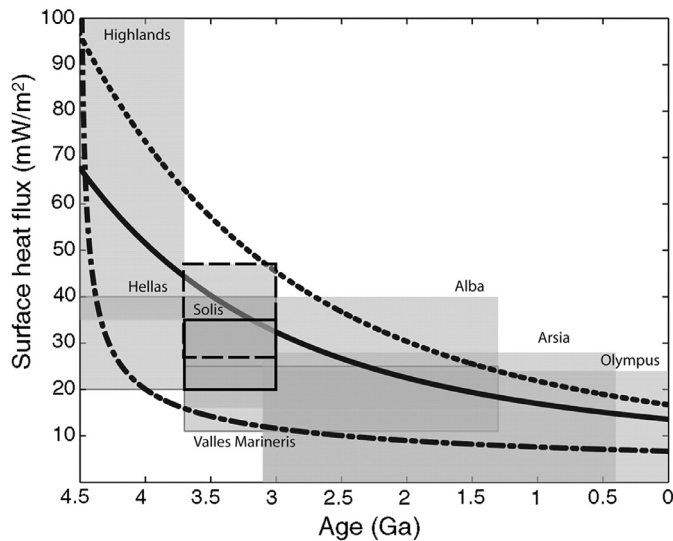


Fig. 1. Estimates of Martian heat flux versus time. Boxes are representative of the Martian heat flux derived from lithosphere modeling of specific features. Curves display the results for models of the thermal evolution of Mars. From Solomon et al. (2005).

along with the pressure gradient generated by the crustal thickness variations may induce lower crustal flow (e.g., Nimmo and Stevenson, 2001; Mohit and Phillips, 2006, 2007; Karimi and Dombard, 2011). The lower crustal flow then moves the material from outside to inside underneath the crater depression and serves to reduce the topography at the crust–mantle boundary. Due to the loss of the isostatic support, the buoyant support of the surface topography transfers to the lithosphere, which results in an upwards flexural response and shallowing of the crater. Indeed, previous studies have shown the major role of the viscoelastic relaxation on the evolution of lunar basins (e.g., Neumann et al., 1996; Mohit and Phillips, 2006), as well as on Mars (Mohit and Phillips, 2007). There are shortcomings with these initial analyses, however. For instance, Dombard et al. (2007a) have demonstrated the important role of the remnant impact heat in the deformation of large craters. Furthermore, the ages of the studied basins were not well constrained.

In this study, we constrain the heat flux of the Southern Highlands and Northern Lowlands by simulating the lower crustal flow beneath large craters and Quasi-Circular-Depressions (QCDs) (presumably buried craters [e.g., Watters et al., 2006; Frey, 2006]). We employ finite element analysis with a non-linear viscoelastic rheology to simulate the deformation of impact craters at the surface and within the subsurface, and include the effect of remnant impact heat on the local viscosity. Consequently, we are able to place constraints on the thermal evolution of Mars. Since Martian impact craters have a better spatial distribution over the surface of the planet than other isolated geological features, this probe provides a more complete sampling of the thermal history of Mars than previous studies.

2. Martian impact craters

2.1. Identification of the craters

We consider craters and QCDs in the range of ~ 200 – 500 km in diameter. The lower limit is dictated by the resolution of the crustal thickness model of Neumann et al. (2004, 2008), which uses spherical harmonic representations of the gravity and topography of Mars. The MGS95J gravity model of Mars contains spherical harmonic coefficients up to degree and order 95 (newer

versions of gravity models contain coefficients up to degree and order 110); however, the model is only robust to spherical harmonics degree and order 75. Therefore, we limit the smaller end of the craters' size to ~ 200 km, which is intermediate between the full wavelength and half wavelength resolutions of a degree 75 spherical harmonics expansion on Mars. (The gravity and topography models of Mars used in this study are currently available and archived at NASA's Planetary Data System [<http://pds.nasa.gov>].) Several considerations limit the large end of the crater size range. First, we limit the candidates to those with relatively simple histories. For example, the very large Martian basins (e.g., Hellas and Argyre) have gone through many processes (e.g., volcanic infilling, sedimentation, or both) and consequently have complex histories (e.g., Dohm et al., 2015). In addition, the lower crustal flow that we simulate here is a function of the flow channel thickness relative to the horizontal length scales (e.g., Nimmo and Stevenson, 2001). Since the thickness of the channel is relatively small for very large craters, the role of the lower crustal flow is less significant for craters larger than ~ 500 km. Furthermore, the planar approximation used in our simulations would begin to break down for diameters larger than ~ 500 km, necessitating a more complex simulation that includes planetary curvature. Consequently, we constrain the size of our candidate craters to ~ 200 – 500 km.

Impact craters of this scale, with an obvious surface expression in imagery, are virtually absent in the Northern Lowlands so we are restricted to QCDs. By using Mars Orbiter Laser Altimeter (MOLA) data, it is feasible to characterize surface topography and distinguish even subtle topographic features on the surface. Using MOLA data, many QCDs, which cannot be observed in images, have been discovered in the Northern Lowlands and these are generally interpreted to likely be buried impact craters (Frey et al., 1999, 2002; Frey, 2003; Buczkowski et al., 2005a, 2005b).

Thus, we extract craters and QCDs within the size range of ~ 200 – 500 km from an existing crater database (Barlow, 1988) and a QCD database, although not every impact will be a candidate for our study. Among the impacts in the desired size, we select those craters and QCDs that show definitive mantle uplift centered beneath the surface depression. We determine the azimuthally averaged profiles of topography on the crust–mantle boundary using the marscrust3 model of Neumann et al. (2004, 2008), assuming a quarter-degree of latitude resolution (~ 15 km on Mars) for the radial resolution and for computing the azimuthal averages. Consequently, we find 23 craters and 8 QCDs that meet our requirements. Fig. 2 shows the locations of the candidate craters and QCDs. More detailed information on the candidate craters and QCDs is listed in Tables 1 and 2.

2.2. Analysis and interpretation of Martian impact craters

Our simulations require knowledge of the initial shape of the craters. Studies of the geometric properties of smaller fresh craters (e.g., Boyce and Garbeil, 2007; Garvin et al., 2003) have provided information regarding the initial shape of craters at the time of formation (e.g., initial depth and rim height as a function of diameter). All large craters of the size used in this study have been modified to some degree, so fresh craters to constrain initial shape are lacking. Constraints based on smaller craters can be extrapolated; however, these extrapolations could be different from the real initial shape of the basins. Having slightly different initial shapes for large craters can modify the final results of our modeling. To mitigate this uncertainty, we consider a range of initial shapes. Fig. 3 plots the depths of the candidate craters versus their diameter. We extrapolate (dashed line) the depth–diameter curve of smaller fresh craters of Boyce and Garbeil (2007) (solid line). All of our craters are shallower than predicted by this extrapolation. This depth–diameter curve (Boyce and Garbeil, 2007),

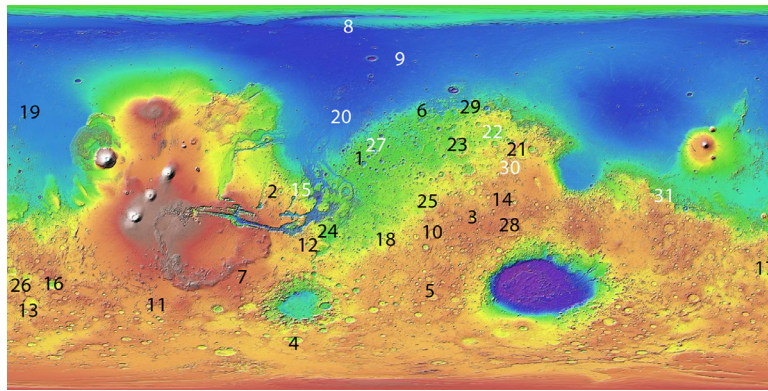


Fig. 2. A topographic map of Mars with the locations of the candidate craters and QCDs. The white digits mark the locations of candidate QCDs, and black digits mark the candidate craters. The digits of impacts are the same that assigned in Tables 1 and 2 and increase based on the size of the impacts.

Table 1

A list of the candidate craters used in this study.

| Latitude | Longitude | Impact name ^a | Impact # | Diameter (km) | Current depth ^a (m) | Impact age (Hartmann) (Ga) | Impact age (Neukum) (Ga) |
|----------|-----------|--------------------------|----------|---------------|--------------------------------|----------------------------|--------------------------|
| 21.79 | 352.06 | Becquerel | 1 | 167.0 | 2500 | 3.64 | 3.87 |
| 0.69 | 304.71 | Mutch | 2 | 180.9 | 1500 | 3.87 | 3.98 |
| −9.30 | 37.92 | Dawes | 3 | 185.2 | 2350 | 3.56 | 3.86 |
| −66.60 | 315.40 | Phillips | 4 | 198.6 | 2400 | 3.88 | 3.97 |
| −46.60 | 19.25 | Kaiser | 5 | 202.8 | 1650–2100 | 4.06 | 4.09 |
| 43.93 | 18.48 | No name | 6 | 203.2 | 1500 | Not datable | Not datable |
| −31.34 | 293.61 | No name | 7 | 205.2 | 900 | Not datable | Not datable |
| −16.94 | 19.16 | Flaugergues | 10 | 228.5 | 1400 | 3.90 | 3.98 |
| −50.45 | 243.53 | Lamont | 11 | 234.4 | 800–1000 | 4.00 | 4.03 |
| −24.98 | 327.89 | No name | 12 | 268.8 | 2250 | Not datable | Not datable |
| −50.01 | 191.12 | Copernicus | 13 | 291.7 | 2150 | 3.91 | 3.97 |
| −2.38 | 56.14 | Schroeter | 14 | 300.0 | 1650 | 3.86 | 3.89 |
| −40.81 | 202.29 | Newton | 16 | 305.6 | 4100 | 3.95 | 4.00 |
| −29.32 | 179.35 | No name | 17 | 340.0 | 1900 | Not datable | Not datable |
| −21.81 | 355.84 | No name | 18 | 384.1 | 1250–1800 | 4.08 | 4.13 |
| 36.80 | 192.61 | No name | 19 | 384.6 | 200 | Not datable | Not datable |
| 21.67 | 60.85 | Antoniadi | 21 | 395.8 | 1500–2000 | 3.83 | 3.89 |
| 23.95 | 31.82 | Cassini | 23 | 435.4 | 2000–2500 | 4.01 | 4.11 |
| −18.41 | 330.62 | No name | 24 | 437.6 | 2000–2300 | Not datable | Not datable |
| −2.54 | 16.68 | Schiaparelli | 25 | 456.5 | 2000–2100 | 3.91 | 3.94 |
| −43.53 | 193.55 | No name | 26 | 460.9 | 1500–2000 | Not datable | Not datable |
| −14.01 | 55.75 | Huygens | 28 | 471.9 | 2400–2700 | 3.99 | 4.01 |
| 41.60 | 38.00 | No name | 29 | 480.0 | 2000 | Not datable | Not datable |

^a Top of the rim to the bottom of the floor.

Table 2

A list of the candidate QCDs used in this study.

| Latitude | Longitude | Impact # | Diameter (km) |
|----------|-----------|----------|---------------|
| 78.09 | 338.76 | 8 | 207.670 |
| 61.50 | 9.88 | 9 | 225.210 |
| 0.64 | 325.36 | 15 | 304.260 |
| 40.70 | 348.08 | 20 | 393.100 |
| 29.88 | 48.39 | 22 | 415.080 |
| 29.37 | 1.29 | 27 | 467.330 |
| 15.16 | 57.46 | 30 | 487.830 |
| −0.15 | 138.75 | 31 | 522.720 |

however, was based on craters smaller than 50 km in diameter. It is thus conceivable that large craters are inherently shallower than this prediction. At a minimum, the initial depths of our craters will be constrained by the depth of the deepest candidate crater, Newton (dotted line in Fig. 3).

As is clear from either curve, the candidate craters all appear much shallower than expected. This apparent alteration could result from either post-impact surficial processes (e.g., surface infilling), the effects of the lower crustal flow, or both. Indeed, Mars has undergone significant surface modification such as fluvial/aeolian erosion and deposition of sediments/volcanic materials since the

Noachian era (e.g., Irwin et al., 2013; Head et al., 2001), and most of our craters are fairly degraded. A significant role for lower crustal flow, however, is indicated by consideration of the degree of isostatic compensation of the craters. Fig. 4 presents the degree of compensation at the crater center versus diameter, based on the current depth versus the current crust–mantle boundary topography of the candidate craters. For each candidate crater, we determine the current mantle topography using the Martian crustal thickness map. We also calculate the anticipated mantle topography in which the very center of the crater is in isostatic equilibrium, and then, compared it versus the current mantle topography at the center of the crater. In these calculations, we assume a crustal density of 2900 kg m^{-3} and a mantle density of 3500 kg m^{-3} (Neumann et al., 2004; Zuber, 2001).

Various studies (e.g., Namiki et al., 2009; Konopliv et al., 2001) suggested that the formation of a large crater on a terrestrial planet should yield a final crater largely compensated in its central regions (i.e., sufficient excess mass from an uplifted dense mantle to compensate the missing mass in the surface topography). If surface infilling was the primary cause for the shallowness of these craters (Fig. 3), without any significant change of the topography on the crust–mantle boundary, then the craters should appear as overcompensated. Our observation, however, indicates that

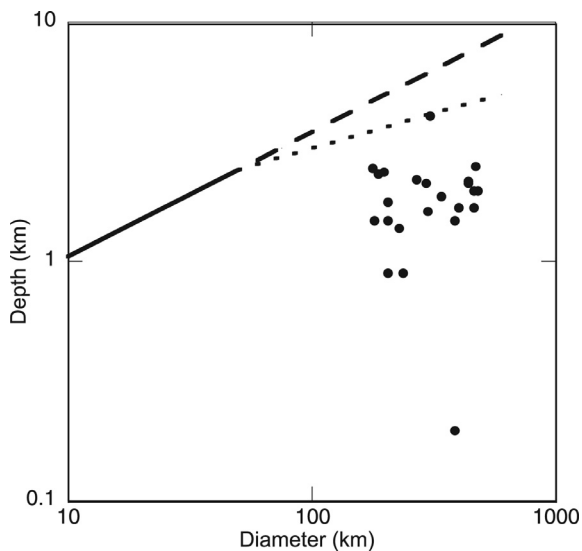


Fig. 3. Plot of the depth versus diameter for the candidate craters. The dashed line is an extrapolation of the depth–diameter curve of small fresh craters of Boyce and Garbeil (2007) (solid line). The dotted line shows an alternate curve constrained by the deepest large crater.

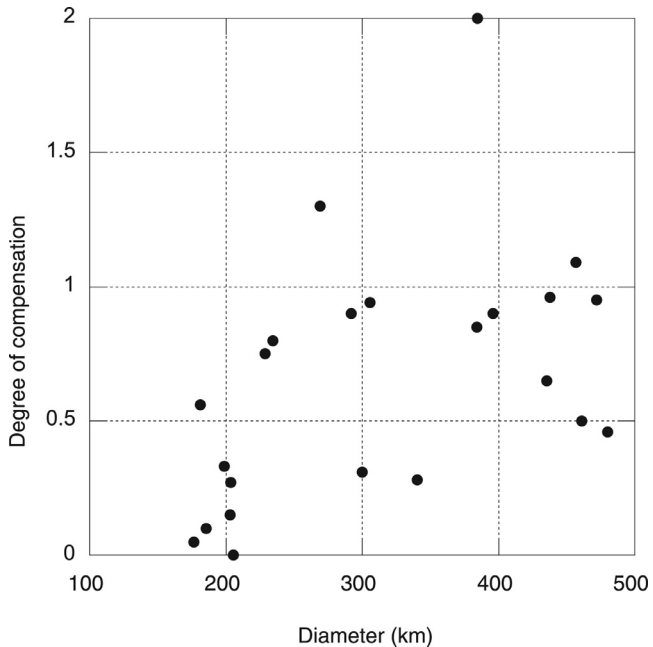


Fig. 4. Degree of center-point compensation versus crater diameter. A degree of compensation equal with 1 means isostatically compensated, while values larger and smaller than 1 are overcompensated and undercompensated. The majority of our candidates are undercompensated, despite generally possessing evidence for surface modification, which suggests lower crustal flow.

our candidate craters are mostly undercompensated (Fig. 4), which strongly implicates lower crustal flow as having a major role in the evolution of the craters. Fig. 4 does show three overcompensated craters, but further investigation shows that their surfaces are heavily eroded. This overcompensation is likely due to the surface infilling/erosion with modest amounts of lower crustal flow.

2.3. Ages of the craters

We employ superposed crater mapping techniques to determine the ages of our candidate craters. The most original-appearing and high-standing regions of these crater rims were mapped in THEMIS

Table 3

Martian geologic epoch age estimates. Taken from Werner and Tanaka (2011) and Michael (2013).

| Epoch | Time (Ga) ^a | Time (Ga) ^b |
|-----------------|------------------------|------------------------|
| Early Noachian | >3.94 | >3.96 |
| Middle Noachian | 3.83–3.94 | 3.85–3.96 |
| Late Noachian | 3.71–3.83 | 3.56–3.86 |
| Early Hesperian | 3.61–3.71 | 3.39–3.56 |

^a Ivanov (2001) chronology used in Neukum system.

^b Hartmann (2005) chronology.

Daytime IR (Christensen et al., 2004; Edwards et al., 2011) and MOLA gridded elevation data (Smith et al., 2001). Superimposed craters down to 1 km in diameter are then extracted from a global Mars crater database (Robbins and Hynek, 2012). Standard crater size–frequency distributions are then created. Regions of each size–frequency distribution that best parallel the two main published isochron systems are then fit, and the ages are calculated (Neukum et al., 2001; Hartmann, 2005; based on the chronology of Ivanov, 2001). (For more details on this method, see Robbins et al., 2013.) Note that using the new chronology of Robbins (2014) would not significantly change the conclusion of this work because most of these large craters formed where Robbins (2014) agrees to within ~200 Ma of Ivanov (2001).

Application of this method allows constraints on the impact age of the candidate craters. According to the Neukum isochron, the age of the impacts are in the range of Early through Mid Noachian. The Hartmann isochron yields an impact age of Early Noachian through Early Hesperian. Both impact-age ranges cover the early eras of Martian history (Table 3). The resultant ages span a fairly limited range of ~0.5 Gyr, with no large candidate craters having formed in the last 3.5 Gyr of Martian history.

The absolute model ages of QCDs cannot be determined via the crater mapping techniques in Robbins et al. (2013). Because of heavy surficial processes and long term burial, the rims of buried craters are not clear; therefore, the absolute age of original impacts cannot be modeled. Frey (2008) has employed $N(50)$ and larger-crater model ages to date large QCDs, but those QCDs are not used here because they greatly exceed our size range. Since QCDs have similar size and spatial distribution as the craters, their originating impacts can be considered to have comparable ages as craters (Frey, 2006). Studies show that the Northern Lowlands of Mars were buried during the early Noachian or even in an earlier epoch before ~4 Ga (e.g., Frey, 2006). Consequently, a minimum impact age of Early Noachian for the QCDs seems reasonable.

3. Methodology

In this study, we use the commercially available MSC Marc-Mentat finite element package (<http://www.mssoftware.com>) to model the viscoelastic relaxation of large Martian craters. Our goal is to determine the range of heat fluxes necessary to permit sufficient lower crustal flow to form the current shape of the crust–mantle boundary beneath candidate craters and QCDs. We employ a two-layer axisymmetric mesh of one radial plane to simulate the surface and subsurface deformation. The basic structure of our mesh is formed of 4-noded quadrilateral elements. In order to minimize the effects of the far edge boundaries on the crater evolution, the side and bottom boundaries are placed three crater radii away (e.g., Dombard and McKinnon, 2006a); we have tested to insure that our results are not sensitive to edge effects at these far boundaries. Following Dombard and McKinnon (2006a), we use a simplified shape for the surface topography, with a 4th order polynomial depression and an ejecta blanket exterior to the rim following an inverse 3rd power law.

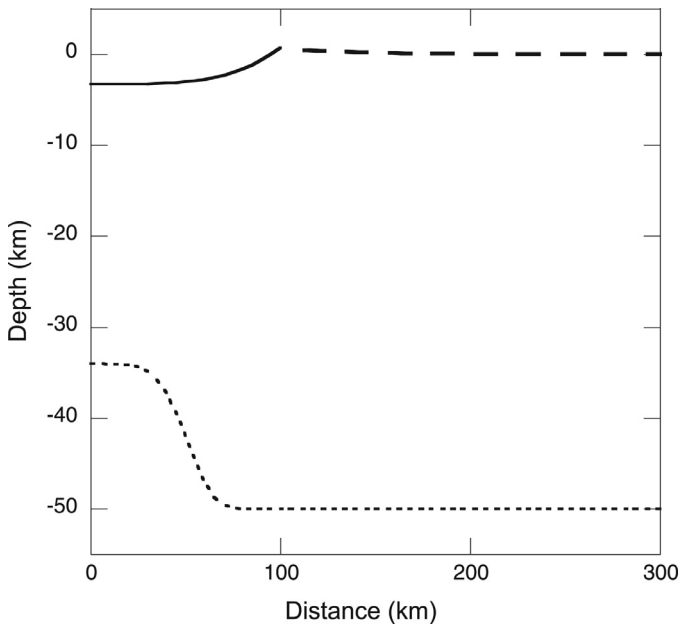


Fig. 5. Plot of the initial crustal profile of a crater ~200 km in diameter. The solid line shows the topography of the depression of the impact crater, the dashed line shows the rim and ejecta blanket, and the dotted line shows the mantle topography.

To determine the shape of the initial uplifted crust–mantle boundary, we implement a Gaussian-like exponential function ($\propto \exp[-r^5]$, where r is radius). This function produces a smooth geometric transition between mantle uplift (underneath the crater depression) and the surrounding flat mantle. We assume the central part of the craters at the surface and subsurface to be in the isostatic equilibrium. The uplifted crust–mantle boundary, however, is narrower than the width of the crater at the surface (e.g., Dombard et al., 2013) and lacks the rim and ejecta topography (Fig. 5). This assumption results in a subsisostatic annulus that surrounds the central mantle uplift. Recent studies facilitated by the high-resolution GRAIL gravity data on the Moon have recognized the presence of an annular subsisostatic region for mascon basins (Andrews-Hanna, 2013; Melosh, et al. 2013; Freed et al., 2014), including some extension of the crust into the mantle at amplitudes far less than the central mantle uplift. Our simulations do not routinely include this crustal extension because the large scale flow to remove the central uplift should not be impeded by this smaller scale feature, a conclusion supported by test simulations.

We consider the width of the mantle uplift at its half maximum to be about ~50% of the crater radius. The gravitational signature of non-mare mascons on the Moon shows that the width of the large positive central free-air gravity anomaly surrounded by a negative free-air gravity anomaly is smaller than the size of the crater (Category C mascons in Dombard et al. 2013). Mantle uplift (beneath a large crater) is primarily caused by the isostatic response of the crust–mantle boundary to the collapsing transient crater, which is narrower than the final crater structure. Post-impact processes affecting the transient crater (e.g., inward and upward collapse) lead to a larger and wider (than the width of mantle uplift) surface basin (Dombard et al. 2013). Furthermore, the central free-air gravity anomalies hover near the isostatic level for these Category C lunar mascons, consistent with the collapse of the transient crater. Those that are subsisostatic are conceivably evolved, while those that appear supersisostatic occur in basins that tend to have basaltic flooding in their central regions. Taken together, our initial shape is reasonable. Furthermore, we also ran a test-simulation with a mantle uplift width of 1.5 times larger than that assumed, and a comparison between the two solutions

showed that the difference between the final results was small (less than 5%). Further tests regarding the initial isostatic state of the central mantle uplift also showed that a slight deviation from isostatic equilibrium does not have a significant effect on the final inferred heat flux.

The results of Garvin et al. (2003) constrained the initial height of the rim. As mentioned in Section 2.2, there are potential uncertainties in the initial depths of large craters. Thus, to determine the initial depth (top of the rim to the floor) of these craters and resolve the problem of uncertainty, we considered two plausible initial depths: deep and shallow. Deep structure is constrained by the extrapolation of the depth–diameter curve of Boyce and Garbeil (2007), and shallow structure is constrained by the depth of the Newton crater (see Fig. 3). These two plausible pathways help us to better picture the initial shape of the craters.

For the shape of the candidate QCDs, we apply a flat surface, with no topography, while the subsurface topography is identical to that of a same sized crater, using both the shallow and deep values. (Initial crustal profiles of all candidate craters and QCDs, for both deep and shallow geometries, are provided in the auxiliary materials.)

In our simulations, the average crustal thickness for craters in the Southern Highlands is 50 km (Zuber, 2001). The average crustal thickness is thinner in the Northern Lowlands (~35–40 km; Zuber, 2001; Zuber et al., 2000). In our simulations however, we consider a background crustal thickness of 45 km for QCDs, slightly thicker than the average, because of the proximity of the candidate QCDs to the crustal dichotomy boundary. Furthermore, we ran a few test-simulations to investigate the sensitivity of the crater deformation to the background crustal thickness.

We assume a crustal density of 2900 kg/m³ and a mantle density of 3500 kg/m³ (Zuber, 2001). These crustal and mantle domains are subdivided into finite element meshes that typically have of order of 10⁴ elements. In our mesh design, a higher resolution is applied to the near basin, while farther from the basin the resolution decreases, resulting in sub-kilometer resolution around the region of primary deformation and tens of kilometers in regions far from the primary deformation. We have confirmed that our results are not sensitive to the exact mesh geometry. With these meshes in hand, we first perform a thermal simulation and input its results as the initial state into a mechanical simulation.

3.1. Thermal solution

Since temperature ultimately controls the viscosity structure within the subsurface, we need to know the thermal state of the system. Here we assume that the thermal system is time-independent; therefore in our study, we do not consider the change of heat flux due to secular cooling of the planet or other temporal effects on the temperature structure. We perform a steady state thermal finite element simulation, finding the conductive equilibrium between a specified basal heat flux and an average surface temperature (heat fluxes on the sides are locked at zero). We assume that the surface temperature is constant and equal with the current average surface temperatures of 210 K, though we test a range of values to examine the effect of this assumed value. The thermal conductivity of the crust and mantle are 2.5 and 4 W m⁻¹ K⁻¹, respectively. In this simulation, we also approximate the thermal effect of remnant impact heat. During a crater's formation, impact heat raises the temperature of the subsurface under the impact site and can result in substantial melting of the near surface material. Consequently, our simulations begin immediately after solidification of any melt (up to ~10 kyr after the impact; Spray and Thompson, 2008), but before substantial dissipation of

the thermal anomaly. To approximate the impact heat in our simulations, we constrain the temperature of the uplifted nodes at the crust–mantle boundary beneath the craters to that of the undeflected crust–mantle boundary far from impact, yielding uplifted isotherms underneath the crater that serve as a proxy for impact heat.

While we run steady state simulations, the actual thermal system is not steady state. In reality, the thermal state changes through dissipation of the impact heat and through secular cooling of the planet. The background heat flux of Mars will change over a characteristic time scale of order 100 Myr (cf. Fig. 1). Additionally, diffusion of an impact thermal anomaly buried tens of kilometers deep also occurs over comparable time scales, assuming a diffusivity of $10^{-6} \text{ m}^2 \text{ s}^{-1}$. As will be demonstrated below, the majority of the deformation occurs relatively early (time scale of up to a few tens of Myr) when driving stresses are highest, so this steady state assumption suffices. Below, we also confirm this assertion with a computationally more expensive simulation that tracks the diffusion of the thermal anomaly, the results of which are nearly identical to those assuming steady state.

3.2. Mechanical solution

Free-slip boundary conditions are applied to the two sides of the mesh, whereas the nodes at the bottom of the mesh are fixed. A vertical gravitational body force with an acceleration of 3.7 m s^{-2} (Mars surface gravity) is applied to the entire mesh. The application of gravity ultimately provides the driving force for the lower crustal flow, as the uplifted crust–mantle boundary (and the surface) seeks to achieve gravitational equilibrium (i.e., a flat interface).

In our simulations, we employ a viscoelastic rheology with no plasticity (a continuum approximation for brittle failure). The elastic parameters are selected to be typical values for crustal and mantle materials (e.g., Turcotte and Schubert, 2014). The nominal elastic Young's moduli for the crust and mantle are 65 and 140 GPa, respectively. The Poisson's ratios for both are 0.25. At this value of the Poisson's ratio, the material is compressible, and the application of a gravitational load will result in self-compaction, with large deviatoric stresses that grow with depth. In order to avoid this gravitational self-compaction, we set the Poisson's ratio to 0.4999, very close to incompressibility limit of 0.5, and we scale the Young's moduli by a factor of 0.8 in order to maintain the flexural rigidity of a lithosphere. Simulations utilizing this incompressibility trick were previously shown to be nearly identical to simulations with a compressible viscoelastic material (cf. Dombard et al., 2007a, 2007b; Dombard and McKinnon, 2006b). The viscous creep rheology of the crust follows the experimentally determined flow parameters for dislocation creep in a wet Maryland diabase (Caristan, 1982). We use a wet rheology, as opposed to a dry one, because of significant and building evidence for water-related activity on early Mars (e.g., Head et al., 2001; Dohm et al., 2009). For the creep rheology of the mantle, we use parameters for dislocation and diffusion creep of a wet natural peridotite (Karato and Wu 1993). We will test our model with dry crustal and mantle rheologies (Mackwell et al., 1998; Karato and Wu, 1993).

Simulations are run for a total model time of 100 Myr, a time sufficient to capture any considerable lower crustal flow and a time after which any unmodeled cooling of the system (due to secular cooling of the interior and diffusion of the impact heat) would retard any further flow. To examine the validity of this time frame, we will test our simulations for longer periods of time, as well as track the diffusion of impact heat over time (see below).

The time steps in the simulation are controlled by the minimum Maxwell time, which is dependent upon the elastic moduli

and viscosity (Turcotte and Schubert, 2014). High temperature promotes low viscosities (consequently smaller Maxwell time), hence, small time steps. As the time step decreases, the required time to finish the simulations becomes longer. In order to keep the running time for simulations of the order of days to weeks, we limit the minimum viscosity to 10^{21} Pa s . We have tested our models with smaller minimum viscosity (e.g., 10^{20} Pa s), which led to the order of magnitude smaller time steps but similar end-model results.

Although strains are typically small, we implement a full large strain formulation, which includes the second-order term of the strain displacement relationship (e.g., Ranalli, 1995) and a geometric update. During the simulation, the mesh geometry changes continuously, and since the topography is the source of stress, updating the geometry is required. Additionally, we apply a constant dilatation scheme that controls numerical errors that yield over-stiff elements while simulating nearly incompressible behavior (e.g., viscous creep).

4. Results

Our study demonstrates the role of the lower crustal flow in the evolution of a large impact crater at the surface and within the subsurface for a sufficiently high background heat flux and thick crust. The pressure gradients generated by crustal thickness variations transfer lower crustal material from the periphery to underneath the crater, thereby reducing the topography at the crust–mantle boundary. In our simulations, we include remnant impact heat, and our results indicate a significant role of that in the deformation, specifically when the basal heat flux is relatively smaller ($40\text{--}55 \text{ mW m}^{-2}$) rather than larger (more than 55 mW m^{-2}). Unsurprisingly, the amount of deformation in the subsurface is larger for a higher background heat flux, due to the lower viscosity of the material. Correspondingly, a thicker crust leads to high temperatures in the lower crust and similar results.

Additionally, the development of lower crustal flow leads to substantial mechanical decoupling of the surface from the subsurface. As the mantle topography relaxes, the negative surface topography of the basin largely loses the buoyant support from the topography on the crust–mantle boundary. Support of the surface topography then must come almost exclusively from a lithosphere thinner than the crust, which results in upward flexure and a reduction in surface topography (Fig. 6). A simulation with no density contrast across the crust–mantle boundary (and hence no buoyant support) further illuminates this concept. While both cases see over a kilometer of shallowing of the surface basin, they are within a few hundred meters of each other.

As the size of the crater increases, the amount of deformation at the crust–mantle boundary is less compared with that of a smaller crater, for the same background heat flux. That is, a larger crater requires a higher heat flux to go through the same amount of relaxation. This result is a common finding of lower crustal flow studies (e.g., Nimmo and Stevenson, 2001), and arises because of the larger lateral distances over which the material must flow for a larger crater.

The basis of our results originates from comparing the current crust–mantle boundary topography beneath the craters with that of our predicted/simulated results. For example, Fig. 7 shows the simulated deformation at the crust–mantle boundary for various heat fluxes versus the current mantle topography and constrains the appropriate background heat flux for the shallowed structure of Basin 17. Since the surface of Mars is subject to alteration via surficial processes, matching the surface topography has secondary value. Using our simulated results, we find the most appropriate heat fluxes that reproduce the current topography at the

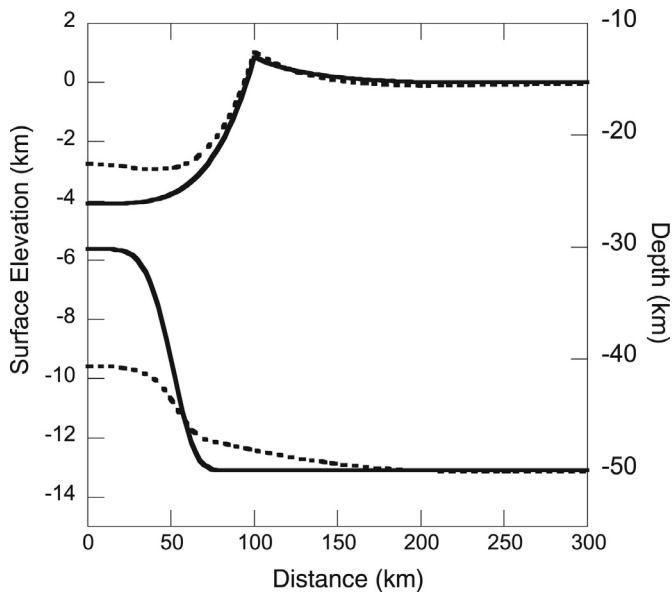


Fig. 6. Simulated topography at the surface and subsurface, versus initial topography. Solid and dotted lines are showing the initial and simulated topography at the surface and crust–mantle boundary.

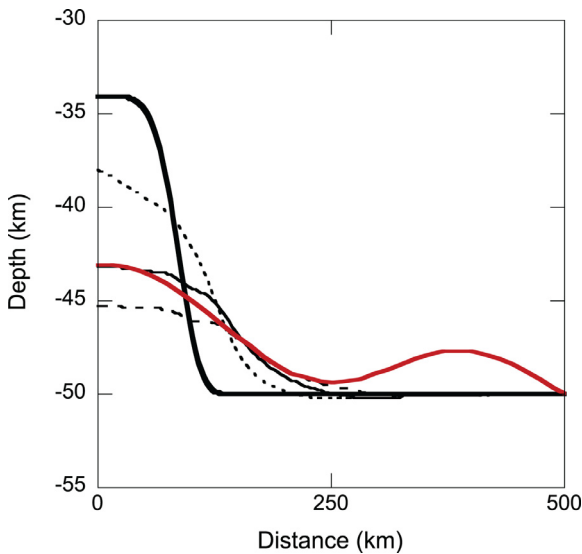


Fig. 7. Simulated subsurface topography for a crater 340 km in diameter (Basin 17). A simulation with a background heat flux of 50 mW m^{-2} (thin black line) produces similar mantle topography beneath the basin center as suggested by the crustal thickness model (red line). For comparison, the simulated topographies with background heat fluxes of 45 (dotted line) and 55 (dashed line) mW m^{-2} are plotted. The bold black line is the initial mantle topography. (For interpretation of the references to colour in this figure legend, the reader is referred to the web version of this article.)

crust–mantle boundary, determined from the crustal thickness model of Neumann et al. (2008). Our study shows that for the majority of candidate craters, a heat flux of 5 mW m^{-2} more than the inferred value relaxes the crust–mantle interface to a noticeably higher degree than that suggested by the crustal thickness model. In contrast, a 5 mW m^{-2} cooler thermal state leads to a smaller amount of relaxation than is required. Therefore, assuming that the other factors such as the rheological parameters are correct, our model determines the appropriate background heat flux with an uncertainty of about $\pm 5 \text{ mW m}^{-2}$. Table 4 lists the inferred background heat flux for the candidate craters and QCDs.

Table 4

List of the candidate craters and QCDs and appropriate background heat flux for them (with an uncertainty of $\pm 5 \text{ mW m}^{-2}$), for both the deep and shallow initial geometries.

| Impact # ^a | Background heat flux (mW m^{-2}) (deep/shallow) | Impact # ^a | Background heat flux (mW m^{-2}) (deep/shallow) |
|-----------------------|--|-----------------------|--|
| 1 | 70/65 | 17 | 55/50 |
| 2 | 50/45 | 18 | 60/55 |
| 3 | 60/60 | 19 | 85/80 |
| 4 | 50/50 | 20 | 80/70 |
| 5 | 60/60 | 21 | 60/50 |
| 6 | 60/55 | 22 | 75/65 |
| 7 | 50/50 | 23 | 65/55 |
| 8 | 60/55 | 24 | 55/50 |
| 9 | 75/70 | 25 | 60/50 |
| 10 | 50/45 | 26 | 75/65 |
| 11 | 55/50 | 27 | $\geq 90/\geq 90$ |
| 12 | 40/40 | 28 | 55/50 |
| 13 | 45/40 | 29 | 80/70 |
| 14 | 65/60 | 30 | $\geq 90/\geq 90$ |
| 15 | 60/55 | 31 | 85/85 |
| 16 | 40/40 | | |

^a cf. Tables 1 and 2.

5. Discussion

5.1. Thermal history

The craters in our study are all, except for one, in the Southern Highlands. QCDs, however, are located in both the Southern Highlands and Northern Lowlands. The combination of these impact craters and QCDs has a fairly even geographic distribution and covers large areas on the surface of Mars (Figs. 3 and 8). The geographical distribution of candidate craters and QCDs, combined with their impact ages, enables us to explore the variation of Martian surface heat flux through space (and time, though to a lesser degree). Fig. 8 shows the location of impacts (QCDs and craters), and the size of the symbols is related to the inferred surface heat flux. Analysis of our candidate craters in the Southern Highlands indicates that the craters closer to the crustal dichotomy boundary formed under a relatively higher background heat flux, with decreasing values farther south of the boundary.

To view further this apparent spatial relationship, we show a thermal contour map (interpolated using the Gaussian method) in Fig. 9. Again, this map shows that the average background heat flux of Mars in the Northern Lowlands was higher than that of the Southern Highlands (during the Noachian), although the relative sparseness of the data points suggest that much of the structure in these contours are artifacts. Consequently, we can illustrate this spatial relationship even more quantitatively by plotting (Fig. 10) the inferred heat flux as a function of distance from the dichotomy boundary (as mapped by Andrews-Hanna et al. (2008)). Although there is noticeable scatter in the heat flow values, there is a clear trend with lower values in the far south and higher values in the Lowlands. We calculate the Pearson correlation coefficients (Press et al., 1992) to assess the relationship between the geographical location of craters (distance from the dichotomy boundary) and associated heat fluxes. Linear fits of the points show R -values of 0.52 (10a) and 0.49 (10b), and p -values of significantly smaller than 0.01, indicating that the geographical location of craters and their associated heat fluxes are correlated.

These observations suggest that a thermal signature from whatever process that formed the crustal dichotomy, which predates the candidate QCDs and craters (Frey et al., 2002), persisted throughout the Noachian. Additionally, the increase in surface heat flux from the Lowlands to the Highlands would seem to preclude formation mechanisms for the crustal dichotomy that put the

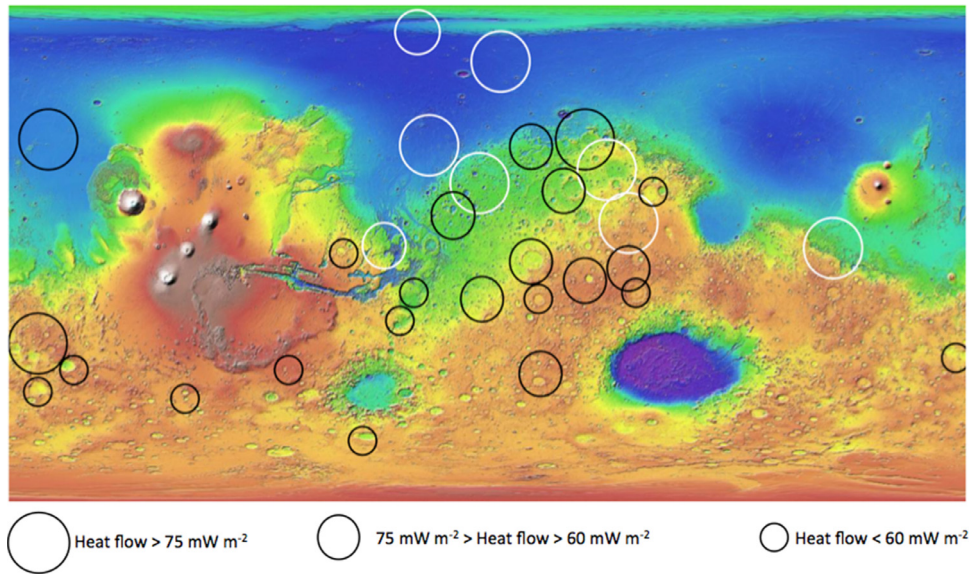


Fig. 8. The inferred background heat fluxes for the candidate craters and QCDs, assuming the deep initial geometry. White and black circles mark QCDs and craters, respectively. As the legend bar shows, large and small circles stand for background heat fluxes of >75 and <60 mW m^{-2} , respectively. Medium size circles represent a background heat flux of $60\text{--}75$ mW m^{-2} . Spatial trends are similar for simulations assuming the shallow initial structure, though the inferred heat flow values are lower.

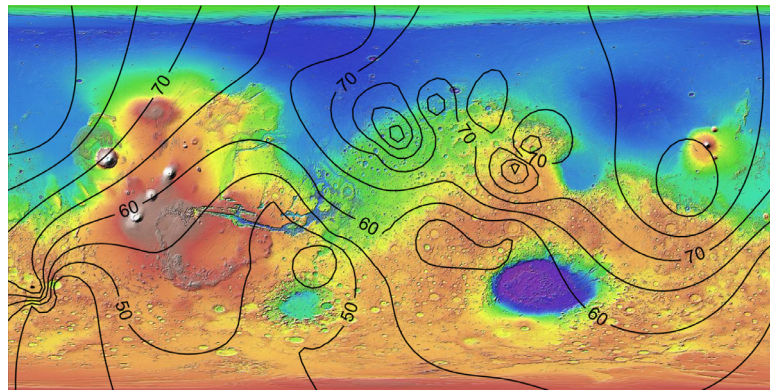


Fig. 9. Contour map of surface heat flux (in mW m^{-2}) of Mars during the Noachian, overlain on the Martian topography and assuming the deep initial geometry. Spatial trends are similar for simulations assuming the shallow initial structure, though the inferred heat flow values are lower.

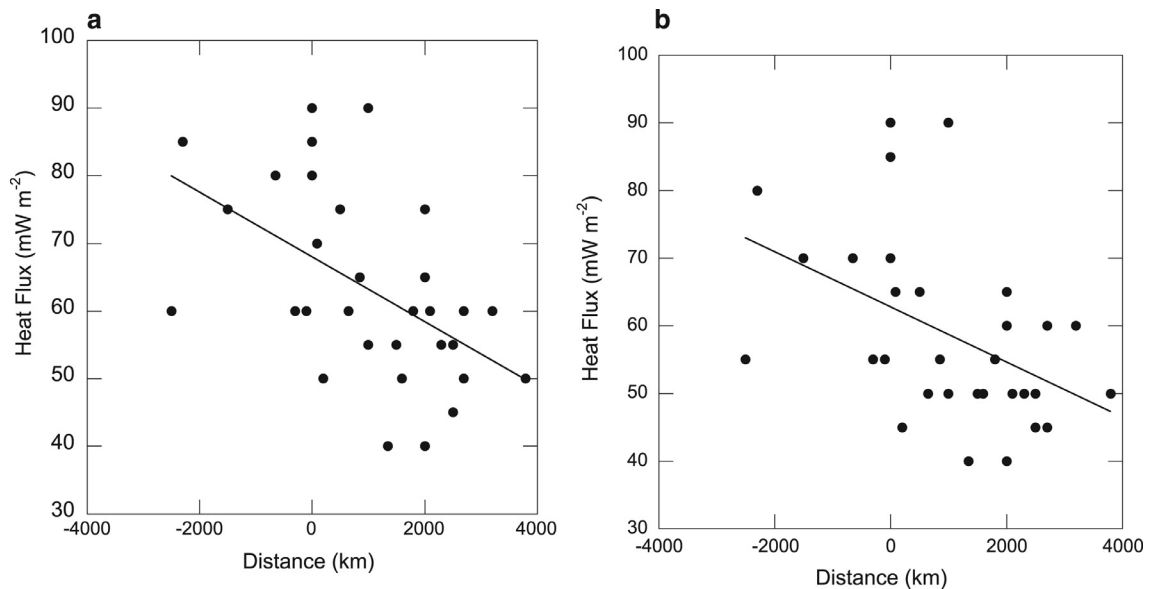


Fig. 10. (a, b) Heat flux versus distance from the dichotomy boundary. Positive values of distance stand for impacts in the Southern Highlands, and negative values stand for impacts in the Northern Lowlands: (a) results using the deep structure; (b) results using the shallow structure. R -values for the line fits are 0.51 (a) and 0.49 (b).

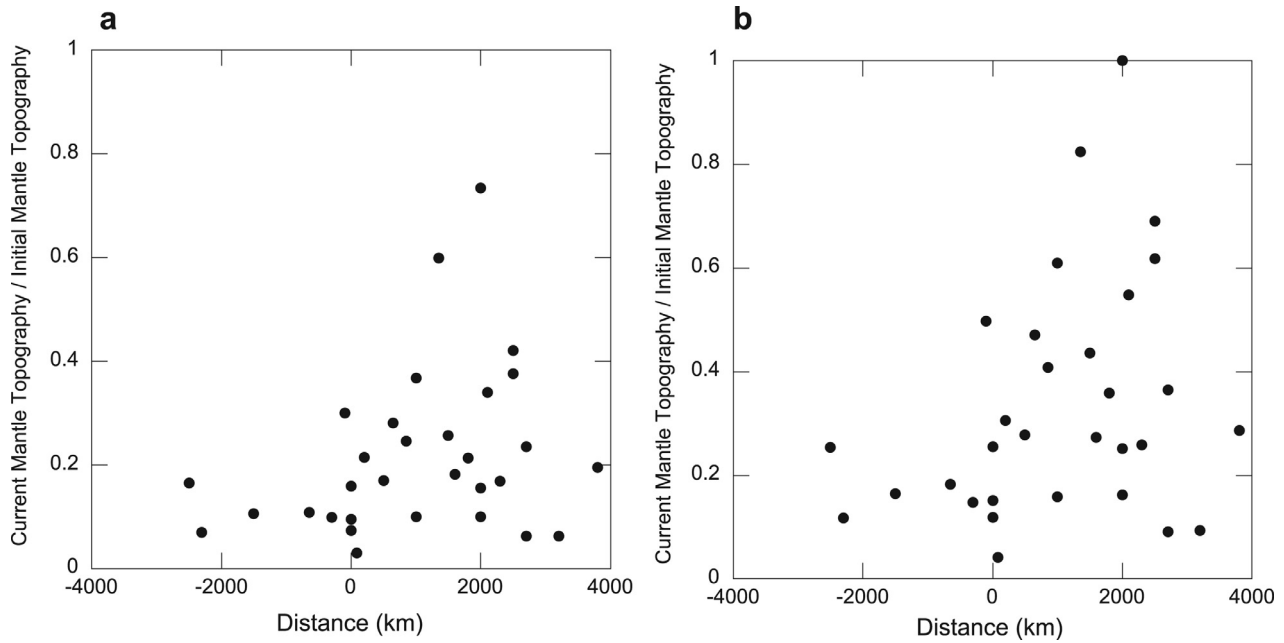


Fig. 11. (a, b) Ratio of current to initial mantle topography underneath impacts versus their distance from dichotomy boundary, for deep (a) and shallow (b) structure.

locus of activity in the southern hemisphere, including degree 1 mantle convection, and mantle overturn (e.g., Roberts and Zhong, 2006; Zhong and Zuber, 2001). This thermal signature would instead seem more consistent with mechanisms that place the locus of activity in the north, including one or several gigantic impacts, removal of the basal lowlands crust by mantle convection, and crustal thinning due to plate tectonics (Andrews-Hanna et al., 2008; Sleep, 1994; McGill and Dimitriou, 1990; Frey and Schultz, 1988; Wilhelms and Squyres, 1984; Wise et al., 1979; Lingenfelter and Schubert, 1973), although we cannot distinguish these remaining mechanisms from our heat flow trends.

This heat flow trend does carry an element of model dependency related to the choices we use in our simulations. We discuss our various tests on the sensitivity of our results to these choices next, but first, we point out here that this trend is also revealed in the observations that guide our simulations. Fig. 11 shows the ratio of the current mantle topography to its predicted initial state for our candidate craters and QCDs as a function of distance from the dichotomy boundary, which again reveals a systematic trend of lower values as one heads from Highlands to Lowlands. This observation is consistent with lower crustal flow, and we have interpreted the heat flows associated with this process. But even if our values are off (or if some other process altogether governs this observation, such as differences in the collapse of the transient craters in the different crustal regimes), this observation shows that some aspect of the crustal dichotomy has affected the morphometry of large Noachian craters.

5.2. Sensitivity tests

The most obvious aspect of our simulations that could affect our results is the choice to use a steady-state thermal structure when the actual thermal structure was time-dependent (i.e., diffusion of the impact thermal anomaly). To begin to understand the impact of this, we plot the evolution of topography on the crust–mantle boundary from one of our simulations that we ran for a period of 200 Myr, longer than our standard time of 100 Myr (Fig. 12). Most of the deformation occurs early (within ~30 Myr), with very small differences for longer times. This behavior is universal among our simulations and arises because the lateral

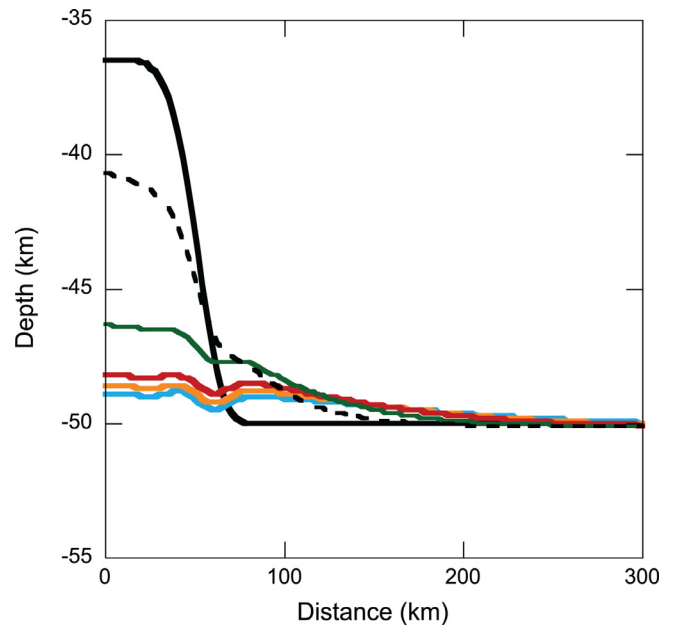


Fig. 12. A demonstration of the deformation at the crust–mantle boundary through time for a crater ~200 km in diameter, with background heat flux of 60 mW m^{-2} . Bold black, dashed, green, red, orange and blue lines show the crust–mantle boundary topography after 0, 10, 30, 70, 100, and 200 Myr, respectively.

pressure gradient that drives lower crustal flow decreases significantly with reduction of the topography on this interface. Over this tens of millions of years time scale, the thermal state is relatively static, suggesting that our implementation of steady state thermal conditions suffices.

To test further the validity of our steady state thermal simulation and demonstrate the role of the lateral pressure gradient in the evolution of a crater, we run a transient simulation in which the impact heat diffuses over time. Fig. 13 presents the simulated mantle topography underneath a crater, ~185 km in diameter, for two cases: (a) impact heat diffuses over time (which is computationally more expensive and time consuming) and (b) a steady state thermal simulation. For the simulation in which the impact

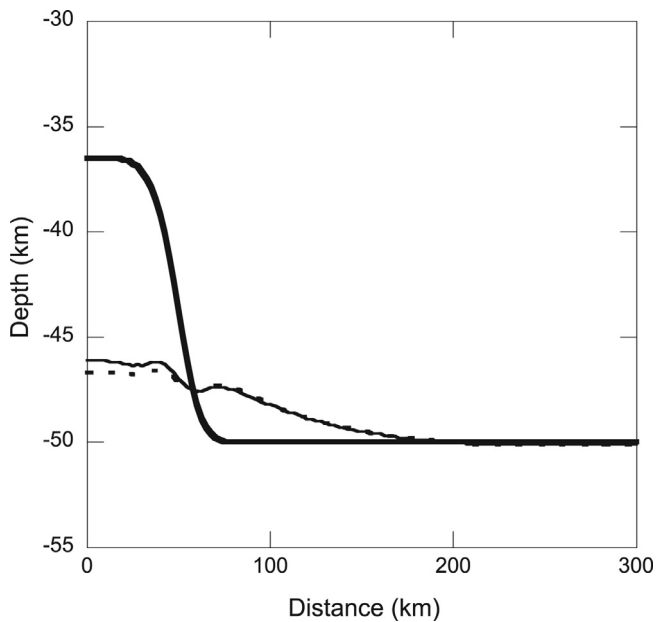


Fig. 13. Relaxation of the crust–mantle boundary topography for two cases with transient (thin line) and steady state (dotted line) thermal simulations at 100 Myr. The background heat flux for both of the simulations is 50 mW m^{-2} .

heat diffuses over time, the relaxation of mantle topography is only slightly less than that of the steady state thermal simulation, which was expected (cf. Fig. 12). This observation justifies the application of a steady state thermal simulation in our study, as well as the evident role of the lateral pressure gradient in the relaxation of these craters.

Another factor controlling the thermal structure is the surface temperature, but the average surface temperature of Mars of 210 K used in this study is likely not universal because of the differing latitudes of the craters and the differing climatic conditions in the distant past. In order to test the sensitivity of our model to changes in surface temperature, we perform a number of simulations with different values, ranging from 180 to 240 K. Results of our simulations (final simulated topography at the crust–mantle boundary) for various surface temperatures are plotted in Fig. 14. Apparent from this figure, the temperature difference of $\pm 30 \text{ K}$ does not have a significant effect on the final results of our simulations. Furthermore, our simulations show that as the background heat flux increases, the effects of the surface temperature on the final topography of the crust–mantle boundary become even smaller.

Geometric effects may also influence our results. For instance in order to explore the thermal evolution of the Northern Lowlands, we have simulated the deformation of large QCDs by modeling no surface topography. It is not certain, however, whether the infilling occurred immediately after the crater formation or at some time after the initial period of several tens of millions of years when lower crustal flow would have been the most prevalent. Thus, we test the effect on the lower crust by simulating a flat surface versus a surface with crater topography. Fig. 15 shows the final topography at the crust–mantle boundary for a QCD and crater of the same size; the difference between the simulated topographies of a QCD and crater at the crust–mantle boundary is relatively small. The QCD, with a flat surface, went through slightly more deformation within the subsurface, likely because of the slightly thicker flow channel. Additional simulations show that as the applied background heat flux increases, the difference between the final topography under a QCD and a crater decreases. Consequently, infilling does not have a significant effect on the process of deformation at the crust–mantle boundary, and this observation stands

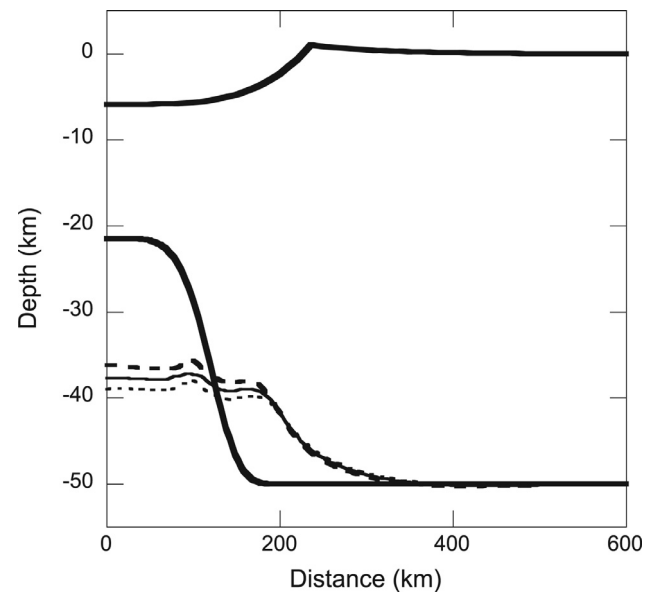


Fig. 14. Effect of surface temperature on lower crustal flow. The bold-solid lines show the initial topography of the Huygens crater at the surface and at the crust–mantle boundary. The dashed, dotted, and thin lines show the simulated crust–mantle boundary for surface temperatures of 180, 240, and 210 K, respectively. The background heat flux is 50 mW m^{-2} .

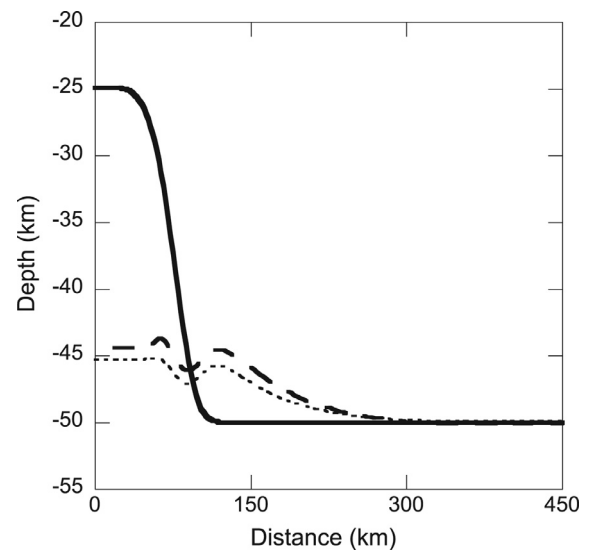


Fig. 15. Differences between the final topography at the crust–mantle boundary for a QCD and crater $\sim 300 \text{ km}$ in diameter and with a background heat flow of 55 mW m^{-2} . The solid line represents the initial topography, while the dashed and dotted lines show the simulated topography of the crater and QCD, respectively.

as further evidence for the mechanical decoupling discussed in the previous section.

Additionally, the majority of the candidate craters are partially (or completely) covered by post-impact sedimentary or volcanic processes, the materials for which likely possess different densities from the crust. This change in crustal density leads to a change in crustal structure and hence the current mantle uplift that we are trying to match. A 10% variation in density of this fill relative to the crust, however, only yields $\sim 0.5 \text{ km}$ difference in the inferred mantle uplift for every 1 km of fill. As is shown in the figures, variations in the amount of mantle uplift on this scale would be a challenge for us to distinguish with our simulations, ultimately leading to the same conclusions.

We generally apply a single value for the nominal crustal thickness of 45 km for the Lowlands and 50 km for the Highlands. Since

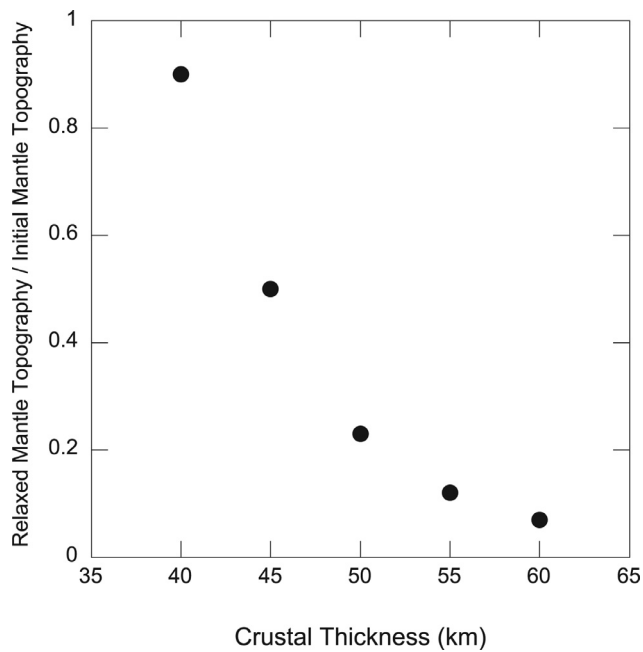


Fig. 16. Ratio of relaxed to initial mantle topography versus crustal thickness. Background heat flux for all of the simulations is 50 mW m^{-2} .

the crustal thickness could be different from place to place, we run simulations to examine the sensitivity with respect to the crustal thickness. Our simulations show that the process of crater deformation is sensitive to the crustal thickness value. Fig. 16 shows the ratio of relaxed to initial topography on the mantle boundary versus crustal thickness for a crater $\sim 200 \text{ km}$ in diameter. As the crustal thickness increases, the amount of relaxation at crust–mantle boundary increases, due to the temperature increase in the lower crust and the larger flow channel thickness. Conversely for a thinner crust, relaxation is less, thus requiring a higher background heat flux. It is significant to note, however, that the hemispherical differences in crustal thickness likely cannot explain the trends seen in the observations (Fig. 11) or our modeled interpretations (Fig. 10) because we would expect to see more relaxation in the Southern Highlands with its thicker crust, which is not the case. The observation of larger mantle topography underneath craters in the Southern Highlands rather than Northern Lowlands (Fig. 11) suggests that regardless of the model sensitivity and modeling choices, the background heat flux should be noticeably higher in the Northern Lowlands.

5.3. Rheology

Our choices for the rheologies can also impact our results. For example, we have assumed that the viscous creep rheology follows the flow rules of a wet material. To test this assumption, we run simulations with the viscous creep parameters determined for anhydrous Maryland diabase and anhydrous Columbia diabase for the crust and anhydrous olivine for the mantle (Mackwell et al., 1998; Karato and Wu, 1993). These results demonstrate that for the same background heat flux, the amount of deformation observed for the dry rheology is significantly less than that of the wet rheology. In other words, our simulations show that an implausibly high heat flux (almost twice as large a background heat flux) would be required in order to reproduce the current topography at the surface and subsurface when dry viscous creep parameters are applied. Thus, this study is consistent with the notion that Mars's interior is wet to certain degree (e.g., Grott and Breuer, 2008).

Additionally, previous analysis of crater relaxation of Ganymede and Callisto showed that plastic deformation (a proxy for

brittle faulting) has no major effect on the final relaxed topography of craters at the surface (Dombard and McKinnon, 2006a). In our study, we apply a viscoelastic rheology with no plasticity, but we tested a few cases with plasticity (effectively applying Byerlee's rule). While the role of plastic deformation because of bending stresses near the surface could affect the final topography of the surface, our results show that plastic deformation does not have any significant effects on the final topography of the crust–mantle boundary.

6. Conclusions

We use the finite element method with a viscoelastic rheological model to simulate the long-term deformation of Martian craters and QCDs at the surface and subsurface. For a sufficiently high background heat flux, lower crustal flow is efficient and reduces the topography at the crust–mantle boundary, and the loss of internal buoyancy results in lithospheric flexure and uplift of the surface topography. We use this phenomenon to determine the appropriate background heat flux for 31 craters and QCDs on Mars, which enables us to produce a thermal map of the Red Planet during the Noachian. Our study shows that in the Southern Highlands, craters closer to the dichotomy boundary experienced a higher background heat flux relative to craters farther from it. In addition, the average background heat flux of the Northern Lowlands is higher than that of the Southern Highlands. This evidence suggests that whatever process formed the crustal dichotomy, its thermal signatures still existed through the Noachian.

Acknowledgments

This was supported by NASA grant NNX08AE98G to A.J.D. We thank Walter Kiefer and Patrick McGovern for reviews that improved the manuscript.

Supplementary materials

Supplementary material associated with this article can be found, in the online version, at doi:10.1016/j.icarus.2016.02.037.

References

- Anderson, S., Grimm, R.E., 1998. Rift processes at the Valles Marineris, Mars: Constraints from gravity on necking and rate-dependent strength evolution. *J. Geophys. Res.: Planets* 103 (E5), 11113–11124. doi:10.1029/98JE00740.
- Andrews-Hanna, J.C., 2013. The origin of the non-mare mascon gravity anomalies in lunar basins. *Icarus* 222 (1), 159–168. doi:10.1016/j.icarus.2012.10.031.
- Andrews-Hanna, J.C., Zuber, M.T., Banerdt, W.B., 2008. The Borealis basin and the origin of the Martian crustal dichotomy. *Nature* 453 (7199), 1212–1215. doi:10.1038/nature07011.
- Banerdt, W., Smrekar, S., Alkalai, L., et al., 2012. INSIGHT: An integrated exploration of the interior of Mars. In: Paper presented at the 43rd Lunar and Planetary Institute Science Conference.
- Barlow, N.G., 1988. Crater size-frequency distributions and a revised Martian relative chronology. *Icarus* 75 (2), 285–305. doi:10.1016/0019-1035(88)90006-1.
- Boyce, J.M., Garbeil, H., 2007. Geometric relationships of pristine Martian complex impact craters, and their implications to Mars geologic history. *Geophys. Res. Lett.* 34 (16). doi:10.1029/2007GL029731.
- Buczkowski, D.L., Frey, H.V., Roark, J.H., McGill, G.E., 2005. Buried impact craters: A topographic analysis of quasi-circular depressions, Utopia basin, Mars. *J. Geophys. Res.: Planets* 110 (E03007). doi:10.1029/2004JE002324.
- Buczkowski, D., Frey, H., McGill, G., 2005. Geographic distribution of QCDs around the northern plains basins of Mars and the relationship to lowland materials. In: *Lunar and Planetary Science Conference*.
- Caristan, Y., 1982. The transition from high temperature creep to fracture in Maryland diabase. *J. Geophys. Res.: Solid Earth* 87 (B8), 6781–6790.
- Christensen, P.R., Jakosky, B.M., Kieffer, H.H., et al., 2004. The thermal emission imaging system (THEMIS) for the Mars 2001 odyssey mission. *Space Sci. Rev.* 110 (1–2), 85–130. doi:10.1023/B:SPAC.0000021008.16305.94.
- Comer, R.P., Solomon, S.C., Head, J.W., 1985. Mars: Thickness of the lithosphere from the tectonic response to volcanic loads. *Rev. Geophys.* 23 (1), 61–92. doi:10.1029/RC023i001p00061.
- Dohm, J.M., Baker, V.R., Boynton, W.V., et al., 2009. GRS evidence and the possibility of paleoceans on Mars. *Planet. Space Sci.* 57 (5), 664–684. doi:10.1016/j.pss.2008.10.008.
- Dohm, J., Hare, T., Robbins, S., et al., 2015. Geological and hydrological histories of the Argire province, Mars. *Icarus* 253, 66–98. doi:10.1016/j.icarus.2015.02.017.

- Dombard, A., Phillips, R., 2010. Viscoelastic finite-element simulations of the flexure under the north polar cap of Mars. In: Paper presented at the *41st Lunar and Planetary Science Conference*.
- Dombard, A.J., Bray, V., Collins, G., et al., 2007. Relaxation and the formation of prominent central peaks in large craters on the icy satellites of Saturn. In: Paper presented at the *39th Bulletin of the American Astronomical Society*.
- Dombard, A.J., Hauck, S.A., Balcerski, J.A., 2013. On the origin of mascon basins on the Moon (and beyond). *Geophys. Res. Lett.* 40 (1), 28–32. doi:10.1029/2012GL054310.
- Dombard, A.J., Johnson, C.L., Richards, M.A., et al., 2007. A magmatic loading model for coronae on Venus. *J. Geophys. Res.: Planets* 112 (E04006). doi:10.1029/2006JE002731.
- Dombard, A.J., McKinnon, W.B., 2006. Elastoviscoplastic relaxation of impact crater topography with application to Ganymede and Callisto. *J. Geophys. Res.: Planets* 111 (E1). doi:10.1029/2005JE002445.
- Dombard, A.J., McKinnon, W.B., 2006. Folding of Europa's icy lithosphere: An analysis of viscous-plastic buckling and subsequent topographic relaxation. *J. Struct. Geol.* 28 (12), 2259–2269. doi:10.1016/j.jsg.2005.12.003.
- Edwards, C., Nowicki, K., Christensen, P., et al., 2011. Mosaicking of global planetary image datasets. 1. Techniques and data processing for thermal emission imaging system (THEMIS) multi-spectral data. *J. Geophys. Res.: Planets* 116 (E10008). doi:10.1029/2010JE003755.
- Freed, A.M., Johnson, B.C., Blair, D.M., et al., 2014. The formation of lunar mascon basins from impact to contemporary form. *J. Geophys. Res.: Planets* 119 (11), 2378–2397. doi:10.1002/2014JE004657.
- Frey, H., 2003. Buried and visible impact basin distribution on Mars: Comparison with magnetization, gravity and crustal thickness models. In: *Seattle Annual Meeting*.
- Frey, H., 2008. Ages of very large impact basins on Mars: Implications for the late heavy bombardment in the inner solar system. *Geophys. Res. Lett.* 35 (L13203). doi:10.1029/2008GL033515.
- Frey, H.V., Roark, J.H., Shockey, K.M., et al., 2002. Ancient lowlands on Mars. *Geophys. Res. Lett.* 29 (10). doi:10.1029/2001GL013832.
- Frey, H., Sakimoto, S.E., Roark, J.H., 1999. Discovery of a 450 km diameter, multi-ring basin on Mars through analysis of MOLA topographic data. *Geophys. Res. Lett.* 26 (12), 1657–1660. doi:10.1029/1999GL000357.
- Frey, H., Schultz, R.A., 1988. Large impact basins and the mega-impact origin for the crustal dichotomy on Mars. *Geophys. Res. Lett.* 15 (3), 229–232.
- Frey, H., 2006. Impact constraints on the age and origin of the lowlands of Mars. *Geophys. Res. Lett.* 33 (L08S02). doi:10.1029/2005GL024484.
- Garvin, J., Sakimoto, S., Frawley, J., 2003. Craters on Mars: Global geometric properties from gridded MOLA topography. In: *6th International Conference on Mars*.
- Grott, M., Breuer, D., 2008. The evolution of the Martian elastic lithosphere and implications for crustal and mantle rheology. *Icarus* 193 (2), 503–515. doi:10.1016/j.icarus.2007.08.015.
- Hartmann, W.K., 2005. Martian cratering 8: Isochron refinement and the chronology of Mars. *Icarus* 174 (2), 294–320. doi:10.1016/j.icarus.2004.11.023.
- Head, J., Greeley, R., Golombek, M., et al., 2001. Geological processes and evolution. *Chronology and Evolution of Mars*. Springer, pp. 263–292. doi:10.1007/978-94-017-1035-0_9.
- Irwin, R.P., Tanaka, K.L., Robbins, S.J., 2013. Distribution of early, middle, and late Noachian cratered surfaces in the Martian highlands: Implications for resurfacing events and processes. *J. Geophys. Res.: Planets* 118 (2), 278–291. doi:10.1002/jgre.20053.
- Ivanov, B.A., 2001. Mars/Moon cratering rate ratio estimates. *Chronology and Evolution of Mars*. Springer, Bern, Switzerland, pp. 87–104. doi:10.1007/978-94-017-1035-0_4.
- Karato, S., Wu, P., 1993. Rheology of the upper mantle: A synthesis. *Science (New Series)* 260 (5109), 771–778. doi:10.1126/science.260.5109.771.
- Karimi, M., Dombard, A., 2011. The evolution of subsurface and surface topography of large craters on Mars. In: Paper presented at the *AGU Fall Meeting Abstracts*.
- Konopliv, A., Asmar, S., Carranza, E., et al., 2001. Recent gravity models as a result of the lunar prospector mission. *Icarus* 150 (1), 1–18. doi:10.1006/icar.2000.6573.
- Lingenfelter, R., Schubert, G., 1973. Evidence for convection in planetary interiors from first-order topography. *Moon* 7 (1–2), 172–180. doi:10.1007/BF00578814.
- Mackwell, S., Zimmerman, M., Kohlstedt, D., 1998. High-temperature deformation of dry diabase with application to tectonics on Venus. *J. Geophys. Res.: Solid Earth* 103 (B1), 975–984.
- McGill, G.E., Dimitriou, A.M., 1990. Origin of the Martian global dichotomy by crustal thinning in the late Noachian or early Hesperian. *J. Geophys. Res.: Solid Earth* 95 (B8), 12595–12605.
- McGovern, P.J., Solomon, S.C., Head, J.W., et al., 2001. Extension and uplift at Alba Patera, Mars: Insights from MOLA observations and loading models. *J. Geophys. Res.: Planets* 106 (E10), 23769–23809. doi:10.1029/2000JE001314.
- McGovern, P.J., Solomon, S.C., Smith, D.E., et al., 2002. Localized gravity/topography admittance and correlation spectra on Mars: Implications for regional and global evolution. *J. Geophys. Res.: Planets* 107 (E12), 5136. doi:10.1029/2002JE001854.
- McGovern, P.J., Solomon, S.C., Smith, D.E., et al., 2004. E07007-correction to “localized gravity/topography admittance and correlation spectra on Mars: Implications for regional and global evolution”. *J. Geophys. Res.: Planets* 109 (7). doi:10.1029/2004JE002286.
- Melosh, H.J., 1989. *Impact cratering: A geologic process*. Research Supported by NASA. Oxford University Press (Oxford Monographs on Geology and Geophysics, no. 11), New York.
- Melosh, H.J., Freed, A.M., Johnson, B.C., et al., 2013. The origin of lunar mascon basins. *Science* 340 (6140), 1552–1555. doi:10.1126/science.1235768.
- Michael, G., 2013. Planetary surface dating from crater size–frequency distribution measurements: Multiple resurfacing episodes and differential isochron fitting. *Icarus* 226 (1), 885–890.
- Mohit, P.S., Phillips, R.J., 2006. Viscoelastic evolution of lunar multiring basins. *J. Geophys. Res.: Planets* 111 (E12). doi:10.1029/2005JE002654.
- Mohit, P.S., Phillips, R.J., 2007. Viscous relaxation on early Mars: A study of ancient impact basins. *Geophys. Res. Lett.* 34 (L21204). doi:10.1029/2007GL031252.
- Montési, L.G., Zuber, M.T., 2003. Clues to the lithospheric structure of Mars from wrinkle ridge sets and localization instability. *J. Geophys. Res.: Planets* 108 (E6), 108. doi:10.1029/2002JE001974.
- Namiki, N., Iwata, T., Matsumoto, K., et al., 2009. Farside gravity field of the Moon from four-way Doppler measurements of SELENE (kaguya). *Science* 323 (5916), 900–905. doi:10.1126/science.1168029.
- Neukum, G., Ivanov, B.A., Hartmann, W.K., 2001. Cratering records in the inner solar system in relation to the lunar reference system. *Space Sci. Rev.* 96 (1–4), 55–86. doi:10.1023/A:1011989004263.
- Neumann, G., Lemoine, F., Smith, D., et al., 2008. Marscrust3-A crustal thickness inversion from recent MRO gravity solutions. In: Paper presented at the *39th Lunar and Planetary Science Conference*.
- Neumann, G., Zuber, M., Wieczorek, M., et al., 2004. Crustal structure of Mars from gravity and topography. *J. Geophys. Res.: Planets* 109 (E08002). doi:10.1029/2004JE002262.
- Neumann, G.A., Zuber, M.T., Smith, D.E., et al., 1996. The lunar crust: Global structure and signature of major basins. *J. Geophys. Res.: Planets* 101 (E7), 16841–16863. doi:10.1029/96JE01246.
- Nimmo, F., Stevenson, D., 2001. Estimates of Martian crustal thickness from viscous relaxation of topography. *J. Geophys. Res.: Planets* 106 (E3), 5085–5098.
- Press, W.H., Teukolsky, S.A., Vetterling, W.T., et al., 1992. *Numerical Recipes in C: The Art of Scientific Computing*, 131. Cambridge University Press, Cambridge, MA, pp. 243–262.
- Ranalli, G., 1995. *Rheology of the Earth*. Springer Science & Business Media.
- Robbins, S.J., 2014. New crater calibrations for the lunar crater-age chronology. *Earth Planet. Sci. Lett.* 403, 188–198. doi:10.1016/j.epsl.2014.06.038.
- Robbins, S.J., Hynes, B.M., 2012. A new global database of Mars impact craters ≥ 1 km. 1. Database creation, properties, and parameters. *J. Geophys. Res.: Planets* 117 (E05004). doi:10.1029/2011JE003966.
- Robbins, S.J., Hynes, B.M., Lillis, R.J., et al., 2013. Large impact crater histories of Mars: The effect of different model crater age techniques. *Icarus* 225 (1), 173–184. doi:10.1016/j.icarus.2013.03.019.
- Roberts, J.H., Zhong, S., 2006. Degree-1 convection in the Martian mantle and the origin of the hemispheric dichotomy. *J. Geophys. Res.: Planets* 111 (E06013). doi:10.1029/2005JE002668.
- Sleep, N.H., 1994. Martian plate tectonics. *J. Geophys. Res.: Planets* 99 (E3), 5639–5655. doi:10.1029/94JE00216.
- Smith, D.E., Zuber, M.T., Frey, H.V., et al., 2001. Mars orbiter laser altimeter: Experiment summary after the first year of global mapping of Mars. *J. Geophys. Res.: Planets* 106 (E10), 23689–23722. doi:10.1029/2000JE001364.
- Solomon, S.C., Aharonson, O., Aurnou, J.M., et al., 2005. New perspectives on ancient Mars. *Science* 307 (5713), 1214–1220. doi:10.1126/science.307.5713.1214.
- Spray, J.G., Thompson, L.M., 2008. Constraints on central uplift structure from the Manicouagan impact crater. *Meteor. Planet. Sci.* 43, 2049–2057. doi:10.1111/j.1945-5100.2008.tb00660.x.
- Turcotte, D.L., Schubert, G., 2014. *Geodynamics*. Cambridge University Press.
- Watters, T.R., Leuschen, C.J., Plaut, J.J., et al., 2006. MARSIS radar sounder evidence of buried basins in the northern lowlands of Mars. *Nature* 444 (7121), 905–908. doi:10.1038/nature05356.
- Watters, T.R., McGovern, P.J., 2006. Lithospheric flexure and the evolution of the dichotomy boundary on Mars. *Geophys. Res. Lett.* 33 (L08S05). doi:10.1029/2005GL024325.
- Werner, S., Tanaka, K., 2011. Redefinition of the crater-density and absolute-age boundaries for the chronostratigraphic system of Mars. *Icarus* 215 (2), 603–607. doi:10.1016/j.icarus.2011.07.024.
- Wieczorek, M.A., Phillips, R.J., 1999. Lunar multiring basins and the cratering process. *Icarus* 139 (2), 246–259. doi:10.1006/icar.1999.6102.
- Wilhelms, D.E., Squyres, S.W., 1984. The Martian hemispheric dichotomy may be due to a giant impact. *Nature* 309, 138–140. doi:10.1038/309138a0.
- Wise, D.U., Golombek, M.P., McGill, G.E., 1979. Tharsis province of Mars: Geologic sequence, geometry, and a deformation mechanism. *Icarus* 38 (3), 456–472. doi:10.1016/0019-1035(79)90200-8.
- Zhong, S., Zuber, M.T., 2001. Degree-1 mantle convection and the crustal dichotomy on Mars. *Earth Planet. Sci. Lett.* 189 (1–2), 75–84. doi:10.1016/S0012-821X(01)00345-4.
- Zuber, M.T., 2001. The crust and mantle of Mars. *Nature* 412, 220–227. doi:10.1038/35084163.
- Zuber, M.T., Solomon, S.C., Phillips, R.J., Smith, D.E., Tyler, G.L., Aharonson, O., Zhong, S., et al., 2000. Internal structure and early thermal evolution of Mars from Mars global surveyor topography and gravity. *Science* 287 (5459), 1788–1793. doi:10.1126/science.287.5459.1788.